Contemporary Mathematics
https://ojs.wiserpub.com/index.php/CM/

UNIVERSAL WISER PUBLISHER

Research Article

Simplified Analytical Formulation for Thermal Behavior Prediction of a PCM-Based Heat Storage System

Tony Karam[1,2*], **Chantal Maatouk**[1], **Elias Al Sarraf**[3,4]

[1] Faculty of Engineering, ESIB Saint Joseph University of Beirut, P. O. Box, 1514, Riad El Solh, Beirut, 1107 2050, Lebanon
[2] School of Engineering, Lebanese International University, Mouseitbeh, Mazraa, Beirut, P. O. Box, 146404, Lebanon
[3] Faculty of Engineering, Lebanese University, Badaro, Museum, Beirut, P. O. Box, 6573/14, Lebanon
[4] School of Engineering, The International University of Beirut, Mouseitbeh, Mazraa, Beirut, 10210, Lebanon
E-mail: tony.karam2@net.usj.edu.lb

Received: 16 July 2025; **Revised:** 22 September 2025; **Accepted:** 16 October 2025

Abstract: The use of Latent Thermal Energy Storage (LTES) systems in Adiabatic Compressed Air Energy Storage (A-CAES) systems is expected to significantly improve the performance of electricity-generating turbines. This improvement is particularly notable when medium- and high-temperature Phase Change Materials (PCM's) are employed as the storage medium. The relevant literature is abundant with analytical formulations that are intended to model the thermal behavior of large-scale PCM-based LTES systems. While these formulations offer valuable insights, they are mostly validated using experimental or theoretical studies conducted on reduced versions of the full-size storage systems. In an attempt to build on existing literature, this paper proposes an analytical model to simulate the thermal behavior of an industrial-scale PCM-based Shell-and-Tube Heat Exchanger (STHE). In this configuration, compressed air flowing in the shell exchanges heat with a medium- or high-temperature PCM stored in the tubes. The analytical model was validated using a series of Ansys® Fluent® Computational Fluid Dynamics (CFD) simulations conducted on a full-scale model using a variety of PCM's. It was demonstrated that the analytical model, which is based on the Kern method, can successfully predict the PCM phase change fraction evolution with a Root Mean Square Error (RMSE) of less than 0.05, and the compressed air outlet temperature with a Mean Absolute Percentage Error (MAPE) of less than 3%, for PCM Stefan numbers less than 2, at a speed 864 times faster than CFD simulations. Hence, the proposed model can serve as a quick remedy for resource-intensive CFD simulations and costly experiments, which further promotes the integration of PCM-based LTES systems into A-CAES systems.

Keywords: phase change materials, latent thermal energy storage, analytical modeling, Ansys® Computational Fluid Dynamics (CFD) simulations, adiabatic Compressed Air Energy Storage (CAES), General Algebraic Modeling System (GAMS) software

MSC: 00A06, 76F60, 80A20, 80A22

DOI: https://doi.org/10.37256/cm.7120267864

Abbreviation

A-CAES	Adiabatic Compressed Air Energy Storage
CAD	Computer-Aided Design
CAES	Compressed Air Energy Storage
CFD	Computational Fluid Dynamics
CH	Charging Mode
DISCH	Discharging Mode
EII	Energy-Intensive Industries
FE	Finite Element
GAMS	General Algebraic Modeling System
HTF	Heat Transfer Fluid
LTES	Latent Thermal Energy Storage
MAPE	Mean Absolute Percentage Error
PCM	Phase Change Material
RMSE	Root Mean Square Error
STHE	Shell-and-Tube Heat Exchanger
TEMA	Tubular Exchangers Manufacturers Association

Symbols

A	Heat transfer area (m^2)
A_s	Crossflow area at or near the shell centerline (m^2)
B	Baffle spacing (m)
$C_{\min}$	Minimum flow stream heat capacity rate (kW/K)
Cp	Isobaric specific heat (kJ/kg·K)
d	Tube diameter (m)
D_e	Shell equivalent diameter (m)
D_s	Shell inside diameter (m)
f	Friction factor
h	Heat transfer coefficient (W/m^2·K)
j_H	Modified Colburn factor for shell-side heat transfer
k	Thermal conductivity (W/m^2·K)
l	Effective tube length of the heat exchanger (m)
m	Mass (kg)
$\dot{m}$	Air mass flow rate or PCM solidification/melting rate (kg/s)
N	Tubes' count in the shell-and-tube heat exchanger
NTU	Number of heat Transfer Units
Nu	Nusselt number
p	Pressure (Pa)
Pr	Prandtl number
P_T	Tube pitch size (m)
$\dot{Q}$	Heat transfer rate (kW)
$\dot{Q}_{\max}$	Maximum heat transfer rate (kW)
r	Tube radius (m)
r_α	Radial distance of the phase change front (m)
R	Air gas constant (287.05 J/kg·K)
Re	Reynolds number

Rt	Thermal resistance (K/W)
Ste	Stefan number
T	Temperature (K)
U	Overall heat transfer coefficient (W/m^2·K)
V	Volume (m^3)

Greek letters

α	Solid or liquid phase fraction
δ	Clearance between tubes (m)
Δp	Pressure drop (Pa)
Δt	Time step size (s)
ε	Instantaneous heat transfer effectiveness
λ	Latent heat (kJ/kg)
μ	Dynamic viscosity (Pa·s)
ρ	Volumetric density (kg/m^3)
σ	Average tube thickness (m)
ϕ	Viscosity correction factor

Subscripts

α	Solid or liquid phase change fraction
air	Compressed air stream
av	Average
b	Bulk
i	Inner, inside surface of heat exchanger tubes
in	Inlet
l	Liquid phase, liquidus
o	Outer, outside surface of heat exchanger tubes
out	Outlet
pcm	Phase change material
s	Shell, solid phase, solidus
t	Time step, tube(s)
w	Wall

1. Introduction

Thermal energy storage systems have been gaining tremendous momentum in the power generation sector due to their crucial role in improving the capacity factor and the overall efficiency of power plants, while reducing greenhouse gas emissions. A lot of attention is being directed towards Latent Thermal Energy Storage (LTES) systems that utilize Phase Change Materials (PCM's), especially when integrated with wind and solar power plants, due to their high energy density and constant storage temperature over extended periods of time. PCM-based LTES systems can offer solid economic benefits. For example, the levelized cost of energy in solar power plants can be reduced if the traditional two-tank molten salt storage system is replaced by PCM-based Shell-and-Tube Heat Exchangers (STHE's) [1].

In view of these advantages, the modeling of various LTES configurations has become abundantly available in the technical literature, with the STHE being among the promising designs, especially in Concentrated Solar Power (CSP) plants. For instance, Tehrani et al. [2] provided optimized designs for a high-temperature PCM-based STHE to be used in a solar thermal power plant. It was demonstrated that these optimized shell-and-tube configurations can compete with the two-tank molten salt sensible heat storage systems conventionally adopted in CSP plants. The storage unit examined in [2] consists of a STHE having the Heat Transfer Fluid (HTF) flowing inside the tubes while the PCM resides in the shell. The HTF and PCM energy equations were discretized using the first-order implicit, backward, finite difference method in a 2-D model. The effective heat capacity method was used to handle the PCM over its phase change range. The computational code developed in the study was validated based on 2 previous theoretical studies, each addressing a model consisting of a single tube with lengths of 1 meter and 1.5 meters respectively.

Tehrani et al. also derived in [3] a general natural convection Nusselt correlation which can be utilized for early design modeling and rough optimization of PCM-based STHE's integrated with CSP plants. The storage unit configuration tackled in [3] is similar to the one adopted in [2]. The correlation was developed based on multiple Ansys® Computational Fluid Dynamics (CFD) simulation trials, each involving a single-tube model with varying radii and lengths (up to 2 meters). The CFD simulation model was validated against a previous experimental work performed on a LTES system composed of only two 40-cm long concentric cylinders having an outer diameter of 44 mm and an inner diameter of 15 mm.

Beyne et al. [4] derived standardized methods for determining technoeconomic performance indicators of LTES heat exchangers, thereby allowing researchers to expedite the assessment of these LTES systems without the need for lengthy experimentation and CFD simulations. The averaged effectiveness-number of transfer units (ε-NTU) and phase change time methods were identified as important predictive models for the performance of LTES systems.

In another study, Pan et al. [5] developed an explicit analytical solution (that is equivalent to the implicit classical Stefan formulation) for the propagation of the solidification front in a modular heat exchanger consisting of a single tube enclosed in a PCM cylindrical shell. The derived analytical solution was validated using an enthalpy-porosity modeling technique, which had been previously validated experimentally.

Rezaei et al. [6] developed a detailed axisymmetric Finite Element (FE) model for a modular LTES system consisting of a high-temperature PCM (Si-Mg) encapsulated in a vertical Silicon-infiltrated Silicon Carbide (SiSiC) tube and a HTF flowing along the axis of the encapsulation in a porous medium (also made from SiSiC). A transient multi-physics framework was developed in COMSOL Multiphysics® to analyze the performance of the modular storage unit. The model couples the Brinkman-Forchheimer equations for fluid flow and a local thermal non-equilibrium formulation for heat transfer. For the PCM domain, the apparent heat capacity method was implemented, while correlations for heat transfer in porous media were used to compute the heat transfer coefficient and pressure drop of the HTF. Validation of the developed FE model was carried out by simply comparing the individual formulations and methods presented in the study to the corresponding data available in the published technical literature.

In the same context, high-temperature PCM's are seriously viewed as potential game changers in thermal energy storage systems. In their comprehensive review of thermal energy storage technologies for CSP applications, khan et al. [7] concluded that next generation CSP plants will need to target operating temperatures above 700 °C in order to enhance energy density and overall system efficiency. Similarly, an exergoeconomic study conducted on a solar-driven trigeneration system producing electricity, cooling, and freshwater, showed that continuous operation of the solar system would be possible when integrating a high-temperature PCM storage tank to the trigeneration system [8]. Efforts to enhance thermal performance in industrial systems have been explored in various contexts, including computational analyses of complex fluid flows and heat transfer, which offer insights into optimizing energy efficiency in high-temperature processes [9]. Hence, there is an urgent need to fully exploit the potential benefits of high-temperature PCM-based heat storage systems. With this in mind, Energy-Intensive Industries (EII) appear to be the ideal context in which these potential benefits can be unlocked. In fact, waste heat recovery from EII have been gaining a lot of interest, despite the large gap between the various heat storage options investigated in the literature and the solutions actually implemented [10]. It is also estimated that 45% to 85% of the industrial waste heat can be recovered in LTES systems using inorganic PCM's that are ideal for high-temperature applications [11]. As an example in the ceramics industry, Royo et al. [12] simulated the heat exchange between an air stream flowing through the shell of a STHE at an inlet temperature of 650 °C and a high-temperature inorganic PCM stored in the tubes and having a melting temperature of 885 °C. The PCM heat content was being charged from the ceramic furnace's exhaust gases where temperatures can reach above 1,100 °C. A 3-D finite-difference method was developed in order to simulate the transient heat transfer between the air stream and the PCM, using MATLAB® software. The numerical model was validated against previously reported experimental data obtained from a similar but smaller STHE containing a medium-temperature PCM and water as the HTF.

Only outlet temperature profiles were compared for the sake of model validation, i.e., without any verification reported for the phase change front evolution.

The utilization and conversion of waste heat was also investigated by Li et al. [13] who simulated the integration of a cascaded latent heat storage system with a 420-MW combined-cycle gas turbine. During the charging operation, waste heat from the turbine's exhaust gases would be captured by the latent heat storage system. During the discharge operation, the stored latent heat is used to produce high-temperature high-pressure steam for the steam turbine. The LTES system envisaged in the study consisted of 5,600 sets of 20-meter long concentric tubes filled with four cascaded PCM layers in between the tubes. The LTES system was modeled using a 3-D FE formulation which was incorporated into Aspen Plus®, using an explicit discretization scheme. A modular unit consisting of one set of concentric tubes was the subject of the FE formulation. The study presented important findings but not enough details were provided concerning the validation of the proposed FE formulation, neither was there a reference to the correlations used for convective heat transfer between the PCM's and the HTF's.

As can be inferred from the above-presented literature review, the analytical formulations proposed for large-scale PCM-based STHE's resorted to reduced versions of the full-size storage systems, mainly represented by only a single short-length tube, enclosed in a relatively small diameter shell. Furthermore, these analytical formulations were validated using experimental or theoretical studies previously conducted on similar reduced-scale models.

While the above studies offered valuable insight into the thermal behavior prediction of PCM-based LTES systems, most research has concentrated on their integration into CSP plants or EII. There has been relatively little investigation into incorporating these PCM-based LTES system directly with electricity-generating turbines, for the sake of preheating the turbines' compressed air before it enters the combustion chamber. To the authors' knowledge, the use of latent heat for preheating the gas turbines' compressed air is not quite extensively covered in the technical publications [14]. As a matter of fact, preheating the compressed air is conventionally carried out via sensible heat transfer in a variety of ways: either in a combustion chamber using fuel burners [15] or through heat exchangers using a circulating heat transfer fluid [16, 17] or from combustion exhaust gases [18]. The focus on preheating compressed air arises from its role in Compressed Air Energy Storage (CAES) systems, another form of energy storage that can be coupled to LTES systems integrated with electricity-generating turbines [19]. Amongst the various CAES configurations, Adiabatic CAES (A-CAES) appears to have an appealing potential. In this configuration, air is compressed and stored in a reservoir. The heat generated during compression is captured and stored in a separate storage system. This stored heat is then reused to reheat the compressed air as it is released from its storage during the discharge operation [20].

Consequently, the dynamic performance of a latent thermal storage system where the PCM directly exchanges heat with compressed air remains to be further explored. Therefore, the intent of this paper is to propose and validate an analytical model for the thermal behavior of a utility-scale LTES system in which compressed air exchanges heat with a medium- or high-temperature PCM, in an attempt to build on the existing studies which only tackled reduced versions of the full-size storage system. This work will first present a description of the context in which the LTES system can be employed, followed by a formulation of the analytical model which will simulate the heat exchange in the STHE between compressed air and a set of PCM's having different thermophysical properties. Then, a CFD simulation of the full-scale STHE will be carried out on Ansys® Fluent® [21] using the same set of PCM's. The results obtained from the analytical calculations and the Ansys® Fluent® CFD simulations will be assessed and compared in order to validate the analytical model. Once validated, the model can be subsequently used for predicting the thermal behavior of STHE's that employ medium- or high-temperature PCM's, thereby avoiding the need for expensive experimentation and lengthy and resource-intensive CFD simulations.

2. LTES implementation framework

As can be construed from the already presented literature review, the STHE is one of the most widely used heat storage configurations in power plants and will therefore be considered in this research. The STHE that will be simulated in this study is based on the simplified shape of a standard TEMA type-E (one-pass shell) heat exchanger with non-finned tubes. The modeling of the PCM-based STHE will be investigated in the context of the power system shown in Figure 1. The system consists of a wind farm producing electric power in conjunction with a gas turbine in order to meet a certain load demand, in the presence of 2 energy storage systems: an A-CAES and a LTES. The system operates under 2 modes: charging and discharging.

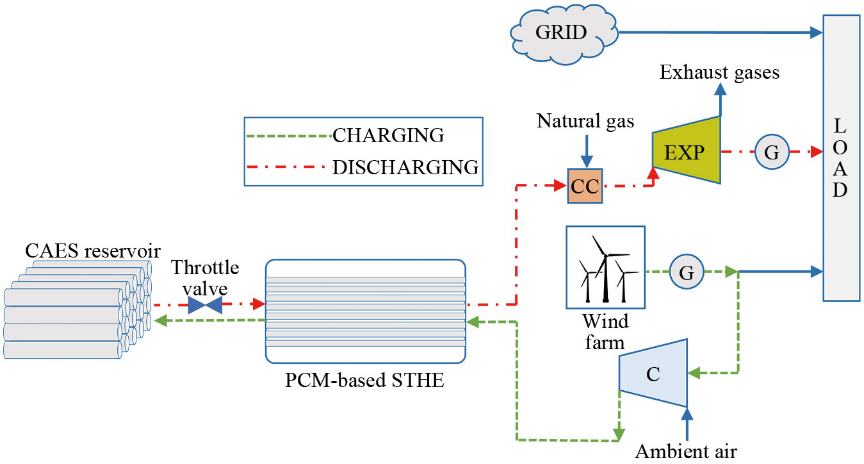

Figure 1. Power system configuration featuring the PCM-based STHE

2.1 *Discharging mode*

When the gas turbine is required to produce electricity (mainly to assist the wind farm during peak load periods), compressed air is released from the CAES reservoir. The temperature of the discharged compressed air would be lower than the air temperature normally expected at the outlet of a gas turbine's compressor. Consequently, the released compressed air will have to be preheated by passing through the PCM-based STHE before entering the turbine's combustion chamber and expander. Therefore, the heat stored in the PCM will be discharged into the compressed air stream, and the PCM will start solidifying.

2.2 *Charging mode*

When the turbine is not operating (during off-peak periods), an auxiliary compressor C will be energized by the wind farm in order to produce compressed air. Before reaching the CAES reservoir, the compressed air flows through the PCM-based STHE where its heat is extracted by the PCM which starts melting.

During both charging and discharging modes, the compressed air stream flows in the shell side of the STHE, while the PCM resides in the heat exchanger's tubes. The interplay between the gas turbine, the A-CAES and the LTES systems appearing in Figure 1 will not be investigated in this work which focuses solely on predicting the thermal behavior of the PCM-based STHE.

2.3 *PCM selection*

A set of medium- and high-temperature PCM's having different thermophysical properties were selected for the simulation calculations of this paper. These PCM's were chosen subsequent to a thorough review of scattered research work on PCM's. The set consists of molten salts belonging to the categories of fluorides, chlorides, nitrates and carbonates. In view of their relevance to utility-scale thermal storage systems (as reported in the technical literature), these PCM's are considered viable candidates for the type of latent heat storage system investigated in this research work. A description of the selected PCM's and their relevance is presented in Table 1. For the composite PCM's, the mass percentage of each constituent is mentioned in the chemical formula. It should also be noted that the corrosivity and stability of the selected

PCM's will not be addressed in this study which focuses solely on the heat exchange calculations in order to validate the use of the proposed analytical model.

Table 1. Selected PCM's & their relevance in thermal energy storage systems

PCM ref.	Composition	Relevant features
PCM1	$MgCl_2$ (63%)- NaCl (23%)-KCl (14%)	Attractive medium-temperature chloride with relatively high heat of fusion [22] Abundant low-cost salt suitable for next generation CSP's (> 700 °C) [23]
PCM2	KCl (61%)-$MgCl_2$ (39%)	Attractive medium temperature chloride with relatively high heat of fusion [22] Suitable as a heat transfer and storage medium in CSP's [24]
PCM3	$MgCl_2$	High-temperature PCM with high heat of fusion suitable for CSP applications (> 750 °C) [25]
PCM4	NaCl	Low-cost high-temperature PCM with high energy density [26] Suitable for high-temperature storage systems (800 °C) and next generation CSP's using supercritical CO_2 power cycles [27]
PCM5	KF (59%)-LiF (29%)-NaF (12%)	High-temperature fluoride salt with high heat of fusion [22] Thermally stable coolant candidate for use in molten salt nuclear reactors [28, 29]
PCM6 PCM7 PCM8	NaF (20%)-ZrF_4 (80%) LiF (16%)-RbF (84%) LiF (31%)-KF (69%)	Coolant candidates for use in advanced high-temperature nuclear reactors [30]
PCM9	K_2CO_3 (34.5%)- Na_2CO_3 (33.4%)- Li_2CO_3 (32.1%)	Carbonate salt suitable for high-temperature LTES applications [22] Thermally stable HTF candidate for use in CSP's operating above 550 °C [31]
PCM10 PCM11 PCM12	Carbonate salt mixtures known as H325, H425 & H525 [32]	Suitable candidates for high-temperature STHE's used in CSP plants [3]
PCM13	KNO_3 (53%)-$NaNO_2$ (40%)-$NaNO_3$ (7%)	Nitrate salt suitable for medium-temperature heat storage applications [22] Coolant candidate for use in molten salt reactors [33]

3. Mathematical modeling of the LTES system

In this section, the analytical mathematical equations and constraints that simulate the discharging and charging modes of the LTES system will be presented.

During the discharge mode, the PCM gives up its heat to the compressed air stream in the shell. It is assumed that the discharge operation starts from full liquid state of the PCM at its liquidus temperature, until full solidification is reached, marking the end of the discharge period. On the other hand, during the charging mode, the PCM initially in full solid state at its solidus temperature, extracts heat from the compressed air stream (produced using renewable wind energy), until a full liquid state is reached. This research work is concerned with the PCM being in phase change state only, i.e., the heat exchange in sensible mode (above liquidus temperature and below solidus temperature) is not tackled in this study.

3.1 *Heat transfer calculations using ε-NTU method*

In line with the findings of [4], The ε-NTU method will be adopted for the calculation of the heat exchange taking place in the STHE. The number of transfer units is expressed in Eq. (1).

$$NTU = \frac{U_o A_o}{1000 \times C_{\min}} \tag{1}$$

where U_o is the overall heat transfer coefficient, A_o is the heat transfer area based on the outside surface of the tubes, and $C_{\min}$ represents the minimum flow stream heat capacity rate for compressed air.

A_o depends on the tube count N, length l, and outer diameter d_o, as shown in Eq. (2), while $C_{\min}$ is evaluated in Eq. (3) based on the compressed air mass flow rate ($\dot{m}_{air}$) and its specific heat (Cp_{air}).

$$A_o = \pi\, d_o\, l\, N \tag{2}$$

$$C_{\min} = \dot{m}_{air}\, Cp_{air}. \tag{3}$$

The heat transfer effectiveness when one of the fluids undergoes a phase change can be expressed as follows:

$$\varepsilon = 1 - exp(-NTU). \tag{4}$$

In this study, the PCM is stored inside the tubes of the heat exchanger and it is assumed that the phase change front moves uniformly towards the center of the tubes during the melting (charging) and solidification (discharging) processes, as illustrated in Figure 2, where r_α corresponds to the radial distance of the phase change front. The movement of the phase change front may not exactly behave as such during the physical process. Nevertheless, the intent is to simplify the modeling of the system's thermal behavior when formulating the analytical model.

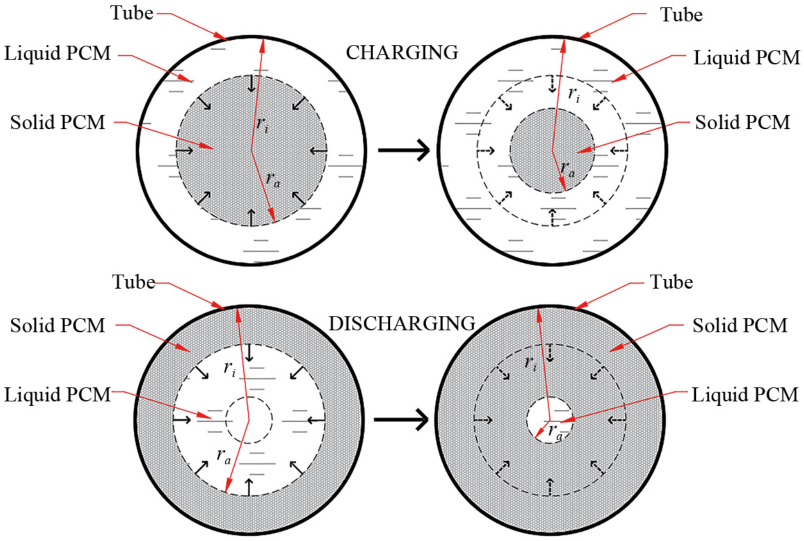

Figure 2. Phase change evolution during melting & solidification

Based on the aforementioned assumption of the phase change front movement and by referring to the geometry of Figure 2, the phase change fraction α which corresponds to the solid fraction α_s (during discharge mode) and the liquid fraction α_l (during charging mode) can be expressed as follows,

$$\alpha = \alpha_s(\text{discharge mode}) = \alpha_l(\text{charging mode}) = \frac{r_i^2 - r_\alpha^2}{r_i^2}. \tag{5}$$

By rearranging the terms in Eq. (5), the ratio $\frac{r_i}{r_\alpha}$ can expressed as follows:

$$\frac{r_i}{r_\alpha} = \frac{1}{\sqrt{1-\alpha}}. \tag{6}$$

During discharge mode, the solidification front propagation of the PCM inside the heat exchanger's tubes will be modelled assuming conduction-only heat transfer inside the PCM without taking into consideration the effect of natural convection. This assumption is reinforced by the fact that the tubes in the heat exchanger are horizontally placed and that their diameter is much smaller than their length. The thermal resistance in the PCM during discharge is therefore associated with heat conduction through the solid phase of the PCM. Conversely, during the charging mode, this thermal resistance is associated with heat conduction through the liquid phase of the PCM.

The PCM thermal resistance Rt_{pcm} will be calculated similarly to the formulation presented by Yang et al. [34] but modified in this research work to account for having the PCM stored inside the tubes rather than in the shell side of the heat exchanger as was the case in [34]. The resulting expression for Rt_{pcm} valid for both modes of operation is given in Eq. (7):

$$Rt_{pcm} = \frac{\ln\left(\frac{r_i}{r_\alpha}\right)}{2\pi\, k_{pcm}\, l} = \frac{-\ln\left(\sqrt{1-\alpha}\right)}{2\pi\, k_{pcm}\, l}. \tag{7}$$

The overall heat transfer coefficient U_o based on the outside surface area of the tubes can therefore be calculated using Eq. (8). The shell-side and tube-side fouling resistances were considered negligible because the analysis assumes regular maintenance of the STHE. Moreover, whenever the PCM reaches its thermal stability limit (an issue outside the scope of this study), it would be replaced, providing an opportunity to clean the heat exchanger surfaces and mitigate fouling.

$$U_o = \left(\frac{1}{h_o} + \frac{r_o\, ln\left(\frac{r_o}{r_i}\right)}{k_t} - \frac{r_o\, ln\sqrt{(1-\alpha)}}{k_{pcm}}\right)^{-1} \tag{8}$$

where

$$r_o = r_i + \sigma. \tag{9}$$

The average tube thickness σ can be inferred from the TEMA dimensional data for heavy-gauge commercial tubing [35]. The thermal conductivity of the PCM is assumed to remain constant during the melting and solidification process. Eq. (10) provides the expression for the maximum possible heat transfer to/from the compressed air during discharge/charge modes:

$$\dot{Q}_{\max} = \dot{m}_{air} \times \left[h\left(T_{pcm}\right) - h\left(T_{air,\ in}\right)\right]. \tag{10}$$

Evaluating the air enthalpy at the constant PCM melting point T_{pcm} is suspected to result in an overestimation of the actual heat transfer between the compressed air and the PCM. A more cautious approach would be to formulate $\dot{Q}_{\max}$ in such a way that the evolving wall temperature T_w is used instead of T_{pcm} when evaluating the air enthalpy, yielding the following modified $\dot{Q}_{\max}$ expression:

$$\dot{Q}_{\max} = \dot{m}_{air} \times \left[h\left(T_W\right) - h\left(T_{air,\ in}\right)\right]. \tag{11}$$

The actual heat transfer rate during the PCM discharge and charging modes is given in Eq. (12):

$$\dot{Q} = \varepsilon \times \dot{Q}_{\max}. \tag{12}$$

The compressed air temperature at the outlet of the heat exchanger during the PCM charging and discharging modes can be evaluated based on $h_{air,\ out}$ in Eq. (13):

$$\dot{Q} = \dot{m}_{air} \times \left[h\left(T_{air,\ out}\right) - h\left(T_{air,\ in}\right)\right]. \tag{13}$$

3.2 *Calculation of the compressed air thermophysical properties*

The thermophysical properties of air will be evaluated based on the bulk mean temperature of air which is taken as the arithmetic mean of the inlet and outlet air temperatures T_{av}. The compressed air when released from the artificial storage system or when produced by compressor C behaves as an ideal gas, in view of the operating temperature and pressure conditions during the charging and discharging modes. Therefore, the air's isobaric specific heat Cp_{air} is not significantly affected by pressure and will only depend on the air bulk mean temperature, as formulated in Eq. (14) taken from [36].

$$Cp_{air} = 1.0484 - 0.3837 \times 10^{-3}\ T_{av} + 0.9453 \times 10^{-6}\ {T_{av}}^2 - 0.549 \times 10^{-9}\ {T_{av}}^3 + 0.0793 \times 10^{-12}\ {T_{av}}^4. \tag{14}$$

The dynamic viscosity and thermal conductivity of air can be expressed as a function of the air bulk mean temperature using a polynomial regression analysis based on the data found in [37], as shown in Eqs. (15) and (16).

$$k_{air} = \left(3.8206 + 0.0798\ T_{av} - 1.6965 \times 10^{-5}\ {T_{av}}^2\right) \times 10^{-3} \tag{15}$$

$$\mu_{b,\ air} = \left(3.4836 + 0.0558\ T_{av} - 1.8431 \times 10^{-5}\ {T_{av}}^2\right) \times 10^{-6}. \tag{16}$$

These expressions make the evaluation of the compressed air properties more convenient when incorporated into a programmable analytical model, eliminating the need to resort to graphs or tabulated data throughout the iterative calculation process.

3.3 *Calculation of the shell-side heat transfer coefficient h_o*

In this part of the research work, a sequence of calculations leading to the evaluation of the shell-side heat transfer coefficient h_o are presented, based on 3 different methods: Kern, Taborek and Bell-Delaware methods. These methods were selected because they are among the most widely adopted and validated approaches for predicting shell-side heat transfer in STHE's [38, 39]. The results of these 3 analytical formulations will then be compared against the results of the CFD simulations conducted on Ansys® Fluent® for the purpose of validating the analytical modeling approach and adopting it whenever quick and rough predictions are required for the thermal behavior of LTES systems.

3.3.1 *Kern method*

The calculations in this section are based on the Kern method [40] and the corresponding mathematical formulations were obtained from [38]. The resulting value of h_o will serve to compute the overall heat transfer coefficient U_o in Eq. (8). The Nusselt number correlation adopted in these calculations corresponds to the one shown in Eq. (17). This correlation is valid for $2,000 \leq Re_{air} \leq 1,000,000$.

$$Nu_{air} = 0.36\, Re_{air}^{0.55}\, Pr_{air}^{\frac{1}{3}}\, \phi_{air}. \tag{17}$$

The Prandtl and Reynolds numbers for compressed air are computed in Eqs. (18) and (19) based on the air properties evaluated at the average bulk temperature in the shell.

$$\underset{air}{\mathrm{Pr}} = 1000 \times \left(\frac{Cp_{air}\, \mu_{b,\, air}}{k_{air}} \right) \tag{18}$$

$$Re_{air} = \frac{\dot{m}_{air}\, D_e}{A_s\, \mu_{b,\, air}}. \tag{19}$$

According to the Kern method, the Reynolds number is based on the equivalent shell diameter D_e and the bundle crossflow area A_s at the center of the shell. The equivalent diameter D_e is calculated along the long axis of the shell and depends on whether a square pitch or a triangular pitch is adopted for the heat exchanger's tubes. A 30° triangular tube layout is generally adopted in the STHE's (unless otherwise dictated by technical requirements) as it results in the highest tube density relative to other layout angles, thereby maximizing the heat transfer area between the compressed air and the PCM [38]. The mathematical expression of D_e for a triangular pitch is presented in Eq. (20).

$$D_e = \frac{4 \times \left(\dfrac{P_T^2\, \sqrt{3}}{4} - \dfrac{\pi d_o^2}{8} \right)}{\dfrac{\pi d_o}{2}}. \tag{20}$$

The bundle cross flow area A_s appearing in Eq. (19) depends on the inside diameter of the shell D_s, the clearance between adjacent tubes δ, the pitch size P_T, and the baffle spacing B, as expressed in Eq. (21). However, in order to mitigate the potential pressure drop of the compressed air stream in the shell (which may be detrimental to the turbine performance), no baffles will be considered in the shell, and the baffle spacing B adopted in the simulation will therefore be set equal to the effective tube length l of the heat exchanger.

$$A_s = \frac{D_s\, \delta\, B}{P_T}. \tag{21}$$

The clearance between the tubes δ is expressed in Eq. (22):

$$\delta = P_T - d_o. \tag{22}$$

The minimum and maximum tube pitches are usually chosen to be 1.25 and 1.5 times the outer diameter of the heat exchanger tubes, respectively [38]. In order to maximize the tube count and the heat transfer area given a certain shell diameter, the tube pitch will be chosen to be 1.25 times the tubes' diameter. The same will also be adopted in the CAD model of the CFD simulation.

$$P_T = 1.25 \times d_o. \tag{23}$$

The air viscosity correction factor ϕ_{air} appearing in Eq. (17) accounts for the large difference between the wall temperature and the compressed air mean bulk temperature, a situation applicable to the context of this study. The viscosity correction factor is calculated in Eq. (24):

$$\phi_{air} = \left(\frac{\mu_{b,\ air}}{\mu_{w,\ air}}\right)^{0.14}, \tag{24}$$

where

$$\mu_{w,\ air} = \left(3.4836 + 0.0558\ T_w - 1.8431 \times 10^{-5}\ {T_w}^2\right) \times 10^{-6}. \tag{25}$$

The wall temperature T_w is taken as the arithmetic mean of the air bulk temperature and the PCM's melting point, as expressed in Eq. (26):

$$T_w = \frac{T_{av} + T_{pcm}}{2}. \tag{26}$$

The shell-side heat transfer coefficient h_o can now be evaluated in Eq. (27):

$$h_o = \frac{Nu_{air}\ k_{air}}{D_e}. \tag{27}$$

The friction factor and the pressure drop experienced by the compressed air in the shell-side are calculated in Eqs. (28) and (29) respectively [38].

$$f_{\text{air}} = \exp\left[0.576 - 0.19 \times \ln\left(Re_{\text{air}}\right)\right] \tag{28}$$

$$\Delta \text{p}_{\text{air}} = \frac{f_{\text{air}}\ \dot{m}_{\text{air}}^2\ D_s}{2\rho_{\text{air}}\ D_e A_s^2 \phi_{\text{air}}}. \tag{29}$$

The air density ρ_{air} is computed in Eq. (30) using the ideal gas law and based on the arithmetic means of the temperature and pressure of the compressed air at the entry and exit of the heat exchanger.

$$\rho_{air} = \frac{p_{av}}{R\, T_{av}}. \tag{30}$$

3.3.2 *Bell-delaware method*

In this section, the heat transfer coefficient will be calculated based on the Bell-Delaware method, which takes into consideration the complexity of the shell flow by combining the effect of the various streams observed inside the shell, in addition to the baffle configuration in the shell [38]. This method can be quite lengthy since it involves a lot of details. A simplified version of the Bell-Delaware method presented in [41] will be adopted. It is valid for Reynolds numbers ranging between 10 and 10^6. The average shell-side heat transfer coefficient is given by

$$h_o = j_H \left(\frac{k_{air}}{D_e}\right) \mathrm{Pr}_{air}^{\frac{1}{3}}\, \phi_{air} \tag{31}$$

where j_H is the modified Colburn factor for shell-side heat transfer, expressed as

$$j_H = 0.5\left(1+\frac{B}{D_s}\right)\left(0.08\, Re_{air}^{0.6821} + 0.7\, Re_{air}^{0.1772}\right). \tag{32}$$

In the above expression, the baffle spacing B is set equal to the length l of the heat exchanger tubes (as was done in the Kern method). The Reynolds number is calculated using Eq. (19), based on the equivalent diameter D_e from Eq. (20) and the bundle crossflow area A_s at the center of the shell from Eq. (21).

3.3.3 *Taborek method*

In an attempt to further explore the possibilities available for the heat transfer analytical formulations, a Nusselt number correlation for the shell-side heat transfer coefficient presented by Taborek in [42] will also be considered in this study. This correlation is mainly utilized for very quick estimations and is valid for Reynolds numbers ranging between 2,000 and 40,000. Given the geometry of the STHE and the operating conditions adopted in this study, the resulting compressed air Reynolds numbers are expected to fall within the (10^4-10^5) range. Although the resulting shell-side Reynolds numbers may not always lie within the applicable range of the Taborek correlation, this method would still be relevant, as it broadens the spectrum of the results, allowing for a more comprehensive comparison of the analytical approaches during the validation process.

In the Taborek method, the Reynolds number is based on the tubes' outside diameter d_o and the bundle crossflow area A_s at the center of the shell, as expressed in Eq. (21):

$$Re_{air} = \frac{\dot{m}_{air}\, d_o}{A_s\, \mu_{b,\, air}}. \tag{33}$$

The shell-side heat transfer coefficient h_o is calculated using the following Nusselt correlation by Taborek:

$$Nu_{air} = 0.2\ Re_{air}^{0.6}\ \underset{air}{\overset{\frac{1}{3}}{\mathrm{Pr}}}\ \phi_{air} \tag{34}$$

$$h_o = \frac{Nu_{air}\ k_{air}}{d_o}. \tag{35}$$

3.4 *Tube-side PCM analysis*

The cumulative solidified PCM mass during the discharge operation and the corresponding solid fraction α_s can be monitored at the end of each time step t of the analytical simulation, using the simple formulations of Eqs. (36) and (37), respectively:

$$m_{pcm,\ s,\ t} = m_{pcm,\ s,\ t-1} + \frac{\dot{Q}\ \Delta t}{\lambda_{pcm}} \tag{36}$$

$$\alpha_{s,\ t} = \frac{m_{pcm,\ s,\ t}}{m_{pcm}}, \tag{37}$$

where m_{pcm} corresponds to the total PCM mass calculated from Eq. (38):

$$m_{pcm} = \rho_{pcm}\ V_{pcm}. \tag{38}$$

Likewise, Eqs. (36) and (37) can also be applied during the charging operation in order to calculate the cumulative melted PCM mass $m_{pcm,\ l}$ and the resulting liquid fraction α_l, respectively.

Figure 3 illustrates the process for the analytical model's heat transfer calculations. The analytical model was simulated using General Algebraic Modeling System software (GAMS) [43] for each one of the considered PCM's. At each time step, GAMS solves the set of simultaneous equations depicted in the block diagram of Figure 3 using CONOPT, a solver suited for large-scale mathematical models [44]. The evolution of the phase change fraction α and the compressed air outlet temperature $T_{air,\ out}$ were monitored by advancing the time step and solving the above set of equations during each time step. In order to ensure a fair comparison between the results of the analytical model and the Ansys® numerical simulation, the size of each time step in the analytical model was taken from the flowtime profile of the transient Ansys® Fluent® simulation, which spans over a maximum duration of 3,600 seconds of physical flowtime. In case full solidification or melting is reached in less than an hour, the analytical calculations are halted.

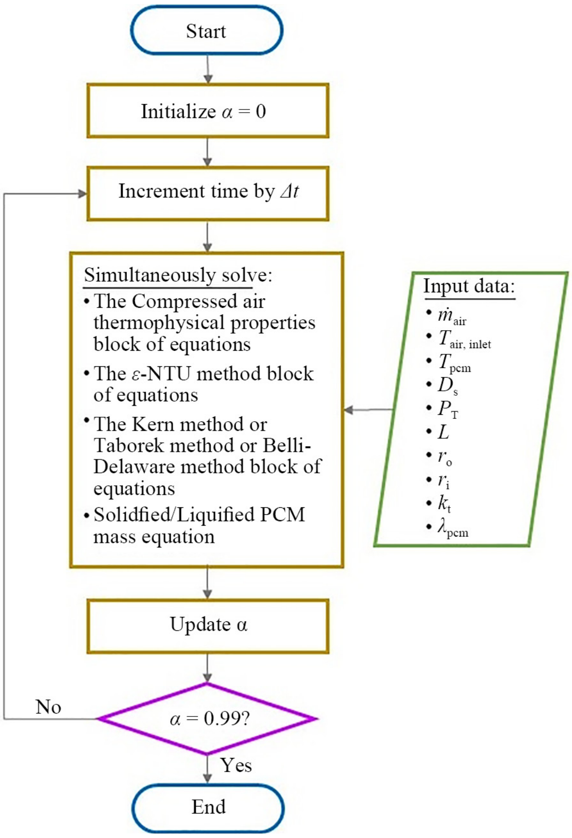

Figure 3. Analytical heat transfer calculations process

4. Ansys® CFD simulation of the LTES system

4.1 *Ansys® model creation*

The proposed analytical model will be validated using the CFD simulation of a 3-D CAD model representing a 5-meter long STHE. The heat exchanger consists of 200 tubes, each with a diameter of 95.6 mm and having a tube pitch of 119.5 mm (1.25 times the tube diameter). As previously justified, a 30° triangular tube layout was adopted. The STHE model was created in Ansys® SpaceClaim® [45] and meshed in Ansys® Fluent® using *Watertight Geometry workflow*. The heat exchanger geometry was based on the simplified shape of a standard TEMA type-E (one-pass shell) heat exchanger with non-finned tubes. In such applications, stainless steel would be selected for the tubes' material due to its ability (amongst other equally suitable alloys) to withstand the corrosive chemical behavior of the PCM's at elevated temperatures, as stipulated in [22]. A 3-D view of the model (along with its physical dimensions) is shown in Figure 4.

It should be noted that resorting to a CFD simulation for the purpose of validating the proposed analytical model was inevitable since physical experimentation with a variety of medium- or high-temperature PCM's in an industrial-scale STHE would be extremely costly and logistically challenging. With this mind, the CFD model had to represent a real-life sized heat exchanger to ensure that the validation of the analytical model was founded on a solid basis. Consequently, the number of cells in the meshed model is expected to be quite high. In order to reduce the computational domain, a symmetry boundary condition was imposed along the longitudinal axis of the STHE reducing its size by half. This modeling approach assumes geometric and flow symmetry while preserving the accuracy of results. Also, a zero-thickness assumption was applied to the 200 tubes in order to further reduce the number of cells in the mesh. The same zero-wall thickness σ was adopted in the analytical model calculations. The surface mesh element size was set to a minimum of 20 mm and a maximum of 125 mm as recommended by Ansys® Fluent® using *Watertight Geometry workflow*, ensuring that a good quality volume mesh is eventually generated for the model. The 20 mm minimum mesh element size was selected in order to capture the small CAD features in the model. The resulting volume mesh which consists of 2,197,591 cells is shown in Figure 5.

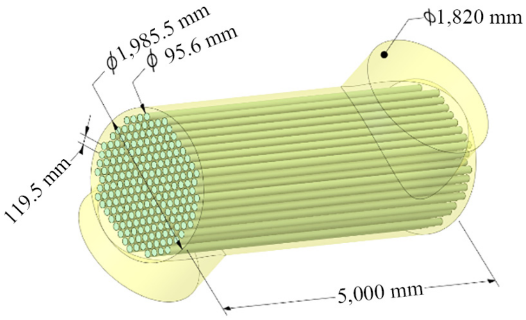

Figure 4. 3-D view of the STHE CFD model

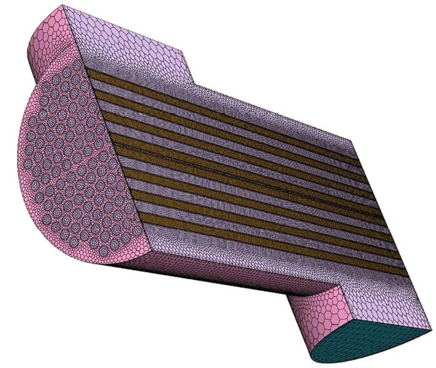

Figure 5. Ansys$^{®}$ Fluent$^{®}$ volume mesh of the axisymmetric CFD model

4.2 *Boundary conditions & materials properties*

The boundary conditions set up for the CFD simulation cases are summarized in Table 2. During the discharge mode, the compressed air mass flow rate and pressure at the inlet of the STHE were based on the mass flow rate and pressure expected in a 14.3-MW simple-cycle SGT-400 gas turbine generator set [46]. The STHE inlet temperature was selected based on the conditions expected in a low-temperature A-CAES system [18] whereby the temperature of the compressed air can be around 350 K as it is released from the artificial CAES reservoir during the discharge operation. During the charging operation, the temperature of the compressed air at the outlet of compressor C (in Figure 1) can exceed 873 K as stipulated in [20]. This 873 K value was chosen to be the compressed air temperature at the STHE inlet, while the mass flow rate and inlet pressure were kept the same as those in the discharge mode. It goes without saying that only the PCM's having a melting point less than the entering compressed air temperature of 873 K should be considered for the charging mode, otherwise PCM melting would not take place.

Table 2. Boundary conditions of the Ansys® Fluent® CFD model

Zone	Type	Condition
Inlet	Mass-flow inlet	22 kg/s, 17 bar, 350 K during discharge mode 22 kg/s, 17 bar, 873 K during charging mode
Outlet	Pressue outlet	-
PCM tubes	Wall	Coupled
Shell surface	Wall	Adiabatic
Symmetry wall	Symmetry	-

The compressed air flowing in the shell was modeled as an ideal gas and its thermophysical properties were expressed as a function of temperature, similarly to what was done in the analytical model. The PCM thermophysical properties were assumed to remain constant throughout the transient simulation and were set as such in Ansys® Fluent® materials properties and the analytical model input data. This is a reasonable assumption since the focus of this study is heat transfer in phase change regime only, where the mass-averaged PCM temperature is not expected to deviate much from the melting/solidification point. The PCM properties are presented in Table 3 ([3, 22–25, 29–32, 47, 48]).

Table 3. Thermophysical properties of the selected PCM's

PCM ref.	T_l K	ρ kg/m^3	μ Pa.s	k W/m·K	Cp kJ/kg	λ kJ/kg
PCM1	658	1,750	0.006	0.95	0.960	461
PCM2	708	2,110	0.006972	0.81	0.80	351
PCM3	987	1,686	0.002188	0.2042	0.9667	454
PCM4	1,073.8	1,557	0.001049	0.5187	1.1922	520
PCM5	727	2,530	0.01235	4.5	1.340	590
PCM6	783	4,110	0.014536	0.357	0.8676	255.39
PCM7	748	3,270	0.000198	0.486	0.8715	230.27
PCM8	765	2,430	0.007758	0.803	2.6551	389.37
PCM9	670	2,300	0.029262	2.02	1.67	276
PCM10	598	2,110	0.0035	0.549	1.505	80
PCM11	698	2,100	0.0035	0.565	1.535	220
PCM12	798	2,350	0.0035	0.565	1.560	155
PCM13	415	2,187	0.00316	0.58	1.560	80

In Table 3, the liquidus temperature corresponds to the PCM melting point reported in the corresponding reference. The solidus temperature in Ansys® Fluent® materials properties was chosen to be 0.1 K less than the liquidus temperature.

4.3 *Transient solution setup & initialization*

For each one of the selected PCM's, a CFD transient simulation was carried out using the pressure-based double-precision solver. The *Solidification & Melting* model was activated and the *Mushy Zone Parameter* set to its default value of 100,000. The *Realizable k-epsilon* turbulent model was adopted for the simulation. With regards to the solution methods and controls, the guidelines suggested in [49] for a solidification-melting problem based on the enthalpy-porosity approach were followed. The same enthalpy-porosity technique is used in the activated *Solidification & Melting* model [50]. Also, *Local Time Step* was chosen as the *Pseudo Time Method* with a specified *Pseudo Time Courant Number* of 5. The CFD simulations were run using adaptive time stepping for a total flowtime of 3,600 seconds. The initial time step size ranged from 1 microsecond to 0.0002 seconds (depending on the simulated case) with growth factors varying between 1.01 and 2, until the step size reached an upper limit of 1 second. Beyond that point, the solution advanced with fixed 1-second steps for the remainder of the transient simulation.

In order to confine the calculation results to the phase change regime, a command was coded into the model to terminate the simulation if complete PCM solidification (or melting) was reached before the end of the 3,600-second duration. This command is triggered whenever the PCM liquid fraction drops below 0.01 during discharge mode or exceeds 0.99 during charging mode.

During discharge mode, each PCM was initialized to be in full liquid state at its liquidus temperature, whereas in charging mode, it was initialized as fully solid at its solidus temperature. Given the horizontal positioning of the PCM tubes and their small diameter relative to their length, the effect of natural convection in the PCM was assumed to be negligible. Accordingly, gravity was not activated and the PCM density was kept constant in the materials properties. If gravity was activated, buoyancy forces would come into play, which creates additional flow patterns that the solver must resolve. This could result in a significant elongation of the simulation time, which would necessitate expensive processing capabilities, an issue that can be addressed in a future study.

4.4 *Grid independence analysis*

In view of the large size of the STHE model, a mesh sensitivity analysis would be required in order to check how the CFD simulation results, namely the evolution of the liquid fraction and the compressed air outlet temperature, would be impacted if the mesh was further refined. To this end, a baseline case was simulated using PCM1 with compressed air mass flow rate of 44 kg/s at 17 bar in discharge mode. Two test cases incorporating finer mesh settings were derived from the baseline case by progressively reducing the minimum and maximum surface mesh element sizes as described in Table 4. The comparison of the results was performed in terms of compressed air outlet temperature MAPE and liquid fraction RMSE, both relative to the baseline case.

As shown in Table 4, the largest deviations occurred in Test Case 2 (finest mesh), with a MAPE of 0.291% for the outlet air temperature and an RMSE of 0.0048 for the PCM liquid fraction. These extremely small deviations are common when the baseline mesh is already close to grid independence, confirming the adequacy of the chosen configuration (minimum surface element size of 20 mm and maximum of 125 mm), which will therefore be adopted for all subsequent simulations. Further refinement to a 10-mm minimum surface element size produced a negligible increase in cell count, suggesting that Ansys® Fluent® meshing algorithm did not impose finer elements because geometric features did not require them. This further supports the choice of the baseline mesh as both accurate and computationally efficient.

Table 4. STHE grid independence analysis results

Case	Min. surface mesh element size (mm)	Max. surface mesh element size (mm)	Volume mesh cell count	Simulation runtime	$T_{air,\ out}$ MAPE	Liquid fraction RMSE
Baseline case	20	125	2,197,591	16 hours 16 minutes	-	-
Test case 1	17.5	110	2,976,614	22 hours 43 minutes	0.162%	0.00261
Test case 2	15	100	4,230,782	34 hours 29 minutes	0.291%	0.0048

5. Analytical model validation

5.1 *Analytical vs. CFD simulations results*

In this section, the results of the analytical and CFD models will be presented and compared for the purpose of validating the analytical model. The analytical and CFD simulations were carried out using an Intel® Xeon® Platinum 8176 server with 16 CPU's, each having 2.10 GHz clock speed. The average simulation run time of the Ansys® Fluent® CFD cases was approximately 24 hours whereas the analytical calculations on GAMS were concluded in 1 minute and 40 seconds.

As stipulated in [4], comparing outlet temperature profiles is not enough to validate the proposed analytical model which should simultaneously predict the phase change fraction evolution. With this in mind, the profiles of the PCM liquid fraction and the compressed air temperature at the outlet of the STHE were compared for each PCM. The comparison of the results will be based on the Mean Absolute Percentage Error (MAPE) of the outlet temperature and the Root Mean Square Error (RMSE) of the liquid fraction which can give an insight into how closely the analytical model can predict the results of the lengthy and resource-intensive CFD simulations. The air outlet temperature MAPE and the phase change fraction RMSE are reported in Table 5 for each analytical method (Taborek, Kern and Bell-Delaware) and for each PCM, during charging and discharging modes. Table 5 also shows the Stefan number associated with each PCM, calculated using Eq. (39). The Stefan number is a dimensionless number that quantifies the relative importance of sensible heat to latent heat during a phase change process. A low Stefan number ($Ste \ll 1$) indicates that the phase change process dominates the sensible heat transfer. When the Stefan number increases, a larger fraction of the heat contributes to sensible heating rather than phase change, indicating a reduced dominance of latent heat effects.

$$Ste = \frac{Cp_{pcm}\left(T_{pcm,\, l} - T_{air,\, in}\right)}{\lambda_{pcm}}. \tag{39}$$

Given the information gap in thermophysical properties for other equally suitable PCM's which could not be included in this study, additional results were generated by varying the Stefan numbers of some of the existing PCM's through changing the inlet air temperature. Furthermore, in addition to the boundary conditions presented in Table 2, various air mass flow rates and inlet pressures were implemented in order to expand the dataset and enhance the validation process, as can be seen in Table 5.

5.2 *Results analysis and discussion*

It can be observed from the results of Table 5 that the MAPE of the compressed air temperature at the outlet of the STHE does not exceed 3% for the Kern and Taborek methods, which is a fairly acceptable value. With regards to the phase change fraction prediction, Figure 6 shows scatter plots of the liquid fraction RMSE values versus the Stefan numbers for each one of the attempted methods (Kern, Taborek and Bell-Delaware). It can be concluded from Figure 6 that the Kern method results exhibited a more noticeable increasing pattern for the liquid fraction RMSE for increasing values of the Stefan number, relative to the other 2 methods. Conducting a linear regression on the results yielded the highest R^2 value for the Kern-based formulation (0.969), making it more suitable to consistently predict the thermal behavior of the STHE in terms of phase change fraction evolution and outlet temperature.

In view of the fact that the phase change fraction varies between 0 and 1, high RMSE values (beyond 0.1) would indicate a poor prediction of the phase change fraction evolution. Therefore, if a conservative maximum RMSE value of 0.05 is tolerated, the Kern-based analytical model will be valid for Stefan numbers not exceeding 2, as can be observed from Figure 6.

This strong correlation between the Kern-based RMSE results and the Stefan number can be attributed to the following: the analytical model simplifies the evolution of the phase change fraction by assuming that the phase change front moves uniformly in the radial direction during each time step. This may reasonably lead to an overestimation of the solidification or melting rate of the PCM. CFD simulations, which aim to capture the underlying physical behavior, are aligned with the analytical model at low Stefan numbers (less than 2) where most of the heat exchanged with the PCM is expected to go into phase change. This could explain the agreement between the analytical and CFD approaches at these low Stefan numbers. The analytical model's predictive accuracy diminishes at higher Stefan numbers, where a smaller proportion of heat goes into phase change; In such cases, the actual phase change progression is slower than the rate predicted by the analytical model which tends to overestimate melting or solidification due to its simplified assumptions.

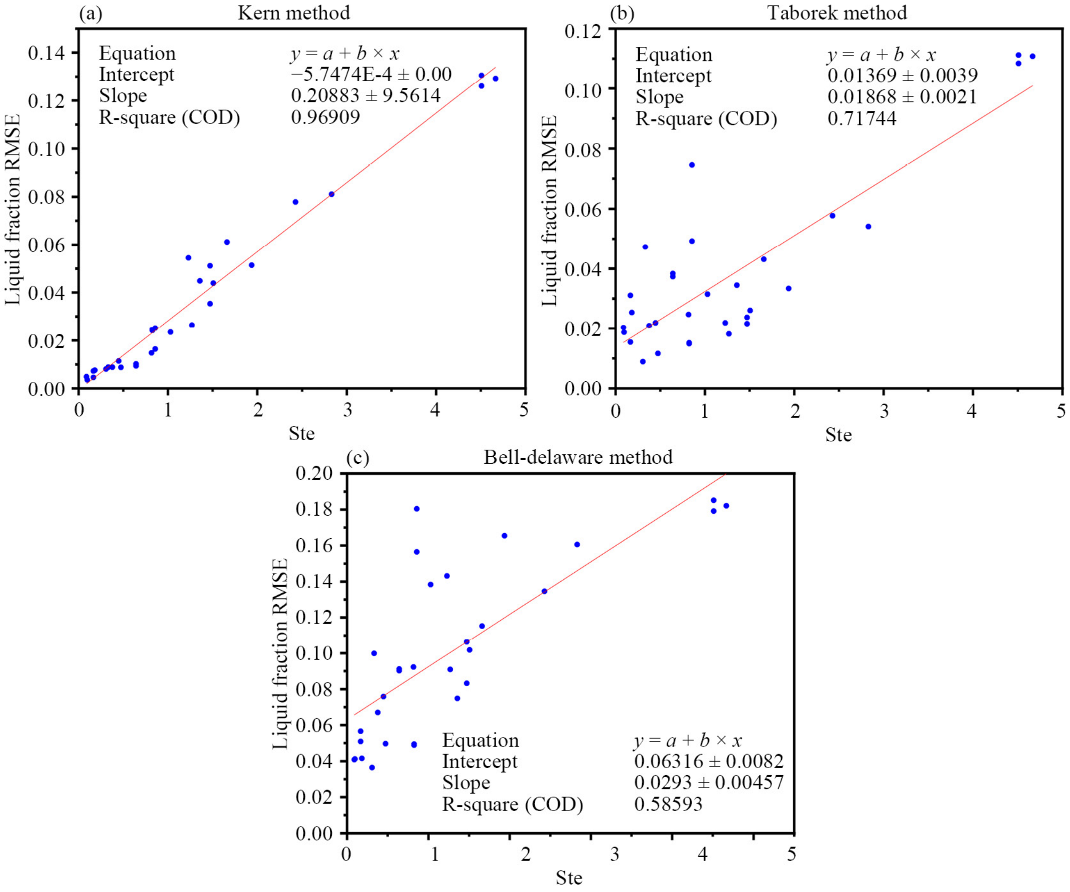

Figure 6. Liquid fraction RMSE vs. Ste number for a) Kern, b) Taborek and c) Bell-delaware methods

While the model's validity for low Stefan numbers might initially seem like a limitation, it is not actually the case, especially during the charging mode. In fact, when a high-temperature PCM is used, the temperature difference between the compressed air and the PCM remains relatively small in charging mode, causing the PCM Stefan number to consistently stay low and thereby enabling the application of the simplified analytical model. This situation is manifested in the results reported in Table 5 for the simulation cases in charging mode.

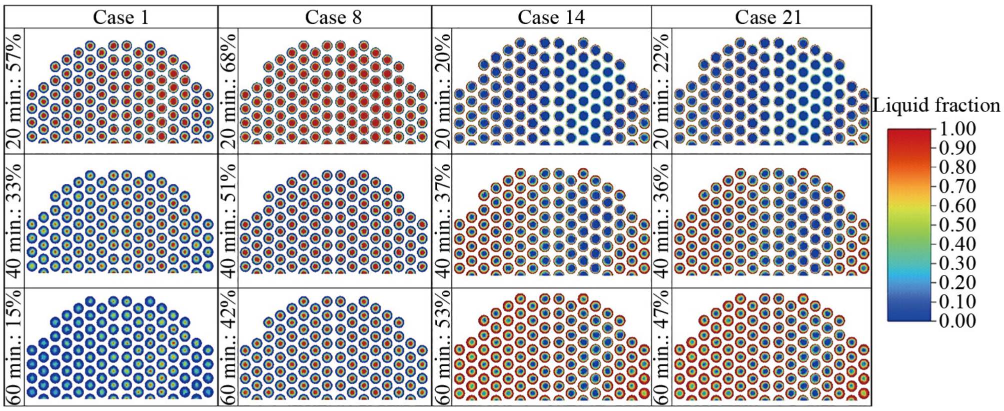

Figure 7. Liquid fraction animation sequences for some simulated cases

Contours of the PCM liquid fraction were created in Ansys® Fluent® on a vertical cross-section at the middle of the STHE in order to monitor the solidification/melting of the PCM's. Figure 7 presents animation frames of these contours captured at 20-minute intervals for some arbitrarily selected simulation cases (with Stefan numbers below 2). The frames clearly illustrate how the solidification (or melting) front progresses radially inward in an almost uniform manner, with only minor deviations. This observed front propagation trend aligns well with the analytical model assumption that the phase change front moves uniformly in the radial direction.

Based on the previously reported simulation runtimes, the analytical modeling approach produced reliable results approximately 864 times faster than the CFD simulations, using the same computational resources.

Concerning the ideal gas behavior assumption for compressed air flowing in the STHE, its validity was assessed by evaluating reduced pressure and temperature values from all the CFD cases. The reduced pressure ranged from 0.318 to 0.663, while the reduced temperature varied between 2.632 and 6.564. These values fall within the region of the generalized compressibility chart where the compressibility factor is almost equal to 1 [36], thereby justifying the assumption of ideal gas behavior.

Both the Kern-based model and the CFD simulations showed that the pressure drop experienced by the compressed air stream flowing through the shell turned out to be quite negligible, not exceeding 0.01% in any of the simulated cases, which further reinforces the validation of the proposed analytical formulation. This negligible pressure drop may be attributed to the low air velocity through the shell cross section, high operating pressures and the short baffle-free flow path, all of which minimize frictional losses. The Reynold numbers resulting from the Kern method analytical calculations are also within the applicable range of the correlation in Eq. (17).

Finally, it should be noted that the validated Kern-based model is only applicable during the phase change process and should not be used to predict the thermal behavior of the PCM during sensible heat transfer. Equally important, both the analytical and CFD models rely on simplifying assumptions. For instance, natural convection effects within the molten PCM and the temperature dependence of its thermophysical properties were assumed to be negligible. These assumptions may introduce discrepancies when compared with real-world system behavior, hence the need for future research to address such effects.

For further illustration of the analytical model validation, the following section will briefly discuss the liquid fraction and compressed air outlet temperature profiles obtained when charging and discharging one of the PCM's (PCM1), using the CFD and analytical models.

5.3 *Case example: PCM1 results*

The profiles of the compressed air outlet temperature and the liquid fraction when employing PCM1 in the STHE are presented in Figure 8 for simulation cases 1 and 3. When the compressed air enters the STHE at 873 K to charge the solid PCM, its temperature at the outlet drops to around 830 K during the first 5 minutes and then starts increasing due to the developing liquid PCM layer shielding the compressed air away from the colder solid PCM. Similarly, during the discharge operation, the compressed air entering the STHE at 350 K exits with a temperature of 400 K for the first 5 minutes. Then this increase in temperature starts diminishing because the PCM thermal resistance starts increasing as the PCM solidifies.

The Kern and Taborek analytical formulations produced satisfactory outlet temperature profiles as can be seen from Figure 8a and Figure 8b, with a MAPE not exceeding 0.3% for Taborek method and 0.6% for Kern method. Furthermore, parts c and d of Figure 8 show that the Kern-based analytical formulation almost exactly predicts the liquid fraction evolution of PCM1, with an RMSE as low as 0.01 in both charging and discharging modes. The phase change front propagation for PCM1 during the charging operation also appears to move radially inward in a nearly uniform fashion with only minor deviations, as shown in the animation frames of Figure 9 (Case 3), much like what was observed in Figure 7 for PCM1 during discharge mode (Case 1).

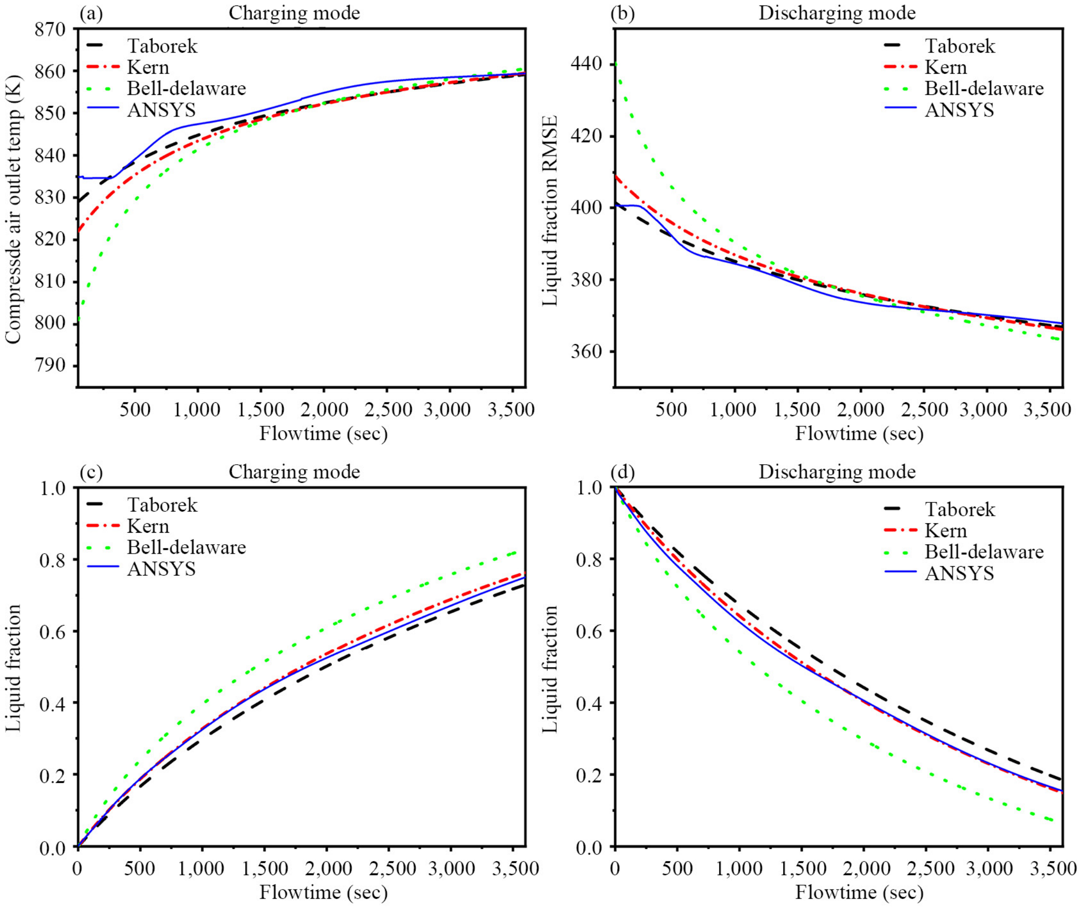

Figure 8. PCM1 liquid fraction evolution & compressed air outlet temperature profile during charging (case 3) & discharging (case 1) modes

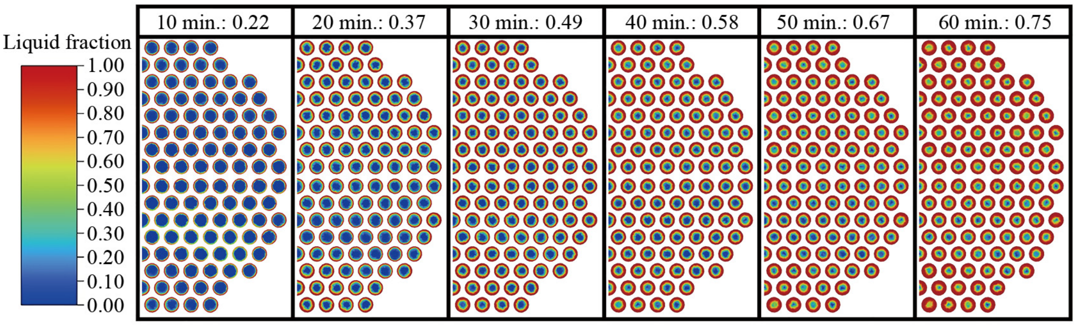

Figure 9. Liquid fraction animation sequences for PCM1 during charging mode (case 3)

6. Conclusions & future research

The intent of this paper was to propose an analytical model that is simple enough to be applied to a full-scale PCM-based STHE for the sake of predicting its thermal behavior without having to resort to lengthy and resource-intensive CFD simulations where the computational burden is commonly remedied by resorting to a reduced version of the model. A set of Ansys® Fluent® CFD simulations were conducted on a full-scale STHE model in order to validate the proposed analytical formulation. It was demonstrated that the analytical model, which is based on the Kern method, was able to successfully predict in less than 2 minutes (864 times faster than the CFD simulations) the phase change fraction evolution with an RMSE of less than 0.05, and the compressed air temperature at the outlet of the STHE with a MAPE of less than 3%, for Stefan numbers below 2. Moreover, both the analytical calculations and CFD simulations showed that adopting a STHE does not result in any significant pressure drop for the compressed air stream, which contributes to promoting the integration of PCM-based STHE's into A-CAES systems coupled to gas turbines.

The validated model can serve as a reliable tool for assessing the thermal behavior of any PCM-based STHE to be integrated with an A-CAES coupled to a gas turbine. The analytical formulation can also be utilized to study the interplay between electricity-generating turbines, the A-CAES and the LTES systems as showcased in the framework of Figure 1. The 3% MAPE for compressed air temperature and 5% RMSE for phase change fraction evolution may be considered acceptable, given the expected operating conditions of this power system. In that same framework, the proposed analytical model can expedite the design and optimal sizing of series and/or parallel combinations of larger-size STHE's especially whenever the durations of the charging and discharging operations need to align closely with the expected wind and electrical load profiles.

It should be noted that reliance on CFD validation has limitations, as the accuracy of the predictions depends on modeling assumptions, boundary conditions, and adopted numerical schemes. While large-scale PCM testing is prohibitively expensive, well-designed experimental work would provide valuable complementary insights, enabling further benchmarking of the numerical model under controlled thermal conditions.

Natural convection in the PCM was not accounted for in the modeling of the LTES system, due to the computational burden that may be faced in the CFD simulations of the STHE CAD model. In fact, this simplification was made to ensure the feasibility of the simulations within the available computational resources and time constraints, as the inclusion of buoyancy-driven flow in the PCM would significantly increase simulation runtime. Future research work could therefore re-evaluate the thermal behavior of the LTES system by taking into consideration the effect of natural convection, in order to capture more accurately heat transfer dynamics and assess the resulting impact on system performance. This could reveal enhanced PCM melting or solidification rates, under variable operating conditions.

Future studies could explore how incorporating temperature-dependent PCM thermophysical properties affects the thermal behavior of the LHS system. In the same context, these studies could also examine the long-term effects of PCM corrosivity and thermal stability on the reliability of the LTES system. In this regard, the evolution of the PCM properties with frequent thermal cycling would help forecast the operational lifespan and maintenance requirements of the PCM-based LTES system, especially under real-world operating scenarios.

Furthermore, future research could investigate the introduction of baffles into the PCM-based STHE to boost the heat transfer between the compressed air and the PCM. However, the presence of baffles may alter the phase change front propagation assumed in this study and increase the pressure drop of compressed air across the heat exchanger. This could result in adverse effects on the performance of the electricity-generating turbine coupled to the system. Accordingly, the trade-off between enhanced heat transfer and air pressure drop must be carefully considered.

Finally, emerging approaches based on machine learning techniques could be explored to potentially accelerate CFD simulations. Computational costs can be dramatically reduced by using data-driven machine learning methods without compromising predictive accuracy. This machine learning approach could therefore complement the analytical formulations when optimizing the design and simulating the operation of PCM-based thermal systems.

Acknowledgement

The financial and computational resources for this research were provided by Saint Joseph University of Beirut.

Conflict of interest

The authors declare no competing financial interest.

References

[1] Prieto C, Cabeza LF. Thermal energy storage with phase change materials in solar power plants. Economic analysis. *Journal of Energy Storage*. 2021; 43: 103184. Available from: https://doi.org/10.1016/j.est.2021.103184.

[2] Tehrani SSM, Taylor RA, Saberi P, Diarce G. Design and feasibility of high temperature shell and tube latent heat thermal energy storage system for solar thermal power plants. *Renewable Energy*. 2016; 96: 120-136. Available from: https://doi.org/10.1016/j.renene.2016.04.036.

[3] Tehrani SSM, Shoraka Y, Diarce G, Taylor RA. An improved, generalized effective thermal conductivity method for rapid design of high temperature shell-and-tube latent heat thermal energy storage systems. *Renewable Energy*. 2019; 132: 694-708. Available from: https://doi.org/10.1016/j.renene.2018.08.038.

[4] Beyne W, T'Jollyn I, Lecompte S, Cabeza LF, De Paepe M. Standardised methods for the determination of key performance indicators for thermal energy storage heat exchangers. *Renewable and Sustainable Energy Reviews*. 2023; 176: 113139. Available from: https://doi.org/10.1016/j.rser.2022.113139.

[5] Pan C, Vermaak N, Wang X, Romero C, Neti S. A fast reduced model for a shell-and-tube based latent heat thermal energy storage heat exchanger and its application for cost optimal design by nonlinear programming. *International Journal of Heat and Mass Transfer*. 2021; 176: 121479. Available from: https://doi.org/10.1016/j.ijheatmasstransfer.2021.121479.

[6] Rezaei E, Barbato M, Ortona A, Haussener S. Design and optimization of a high-temperature latent heat storage unit. *Applied Energy*. 2020; 261: 114330. Available from: https://doi.org/10.1016/j.apenergy.2019.114330.

[7] Khan MI, Asfand F, Al-Ghamdi SG. Progress in research and technological advancements of thermal energy storage systems for concentrated solar power. *Journal of Energy Storage*. 2022; 55: 105860. Available from: https://doi.org/10.1016/j.est.2022.105860.

[8] Abbasi HR, Pourrahmani H. Multi-objective optimization and exergoeconomic analysis of a continuous solar-driven system with PCM for power, cooling and freshwater production. *Energy Conversion and Management*. 2020; 211: 112761. Available from: https://doi.org/10.1016/j.enconman.2020.112761.

[9] Khan MS, Ahmad S, Shah Z, Alshehri A, Vrinceanu N, AL Garalleh H. Computational study of double diffusive MHD natural convection flow of non-Newtonian fluid between concentric cylinders. *Results in Engineering*. 2024; 21: 101925. Available from: https://doi.org/10.1016/j.rineng.2024.101925.

[10] Manente G, Ding Y, Sciacovelli A. A structured procedure for the selection of thermal energy storage options for utilization and conversion of industrial waste heat. *Journal of Energy Storage*. 2022; 51: 104411. Available from: https://doi.org/10.1016/j.est.2022.104411.

[11] Tawalbeh M, Khan HA, Al-Othman A, Almomani F, Ajith S. A comprehensive review on the recent advances in materials for thermal energy storage applications. *International Journal of Thermofluids*. 2023; 18: 100326. Available from: https://doi.org/10.1016/j.ijft.2023.100326.

[12] Royo P, Acevedo L, Ferreira VJ, García-Armingol TJ, López-Sabirón AM, Ferreira G. High-temperature PCM-based thermal energy storage for industrial furnaces installed in energy-intensive industries. *Energy*. 2019; 173: 1030-1040. Available from: https://doi.org/10.1016/j.energy.2019.02.118.

[13] Li D, Hu Y, Li D, Wang J. Combined-cycle gas turbine power plant integration with cascaded latent heat thermal storage for fast dynamic responses. *Energy Conversion and Management*. 2019; 183: 1-13. Available from: https://doi.org/10.1016/j.enconman.2018.12.082.

[14] Karam T, Maatouk C, Al Sarraf E. Impact assessment of combined compressed air and latent heat storage systems on gas turbines. In: *2023 IEEE International Conference on Power Engineering, Electrical and Electronics*. Berlin, Germany: IEEE; 2023. Available from: https://doi.org/10.1109/cpe-powereng58103.2023.10227454.

[15] Vieira FS, Balestieri JAP, Matelli JA. Applications of compressed air energy storage in cogeneration systems. *Energy*. 2021; 214: 118904. Available from: https://doi.org/10.1016/j.energy.2020.118904.

[16] Li Y, Miao S, Yin B, Han J, Zhang S, Wang J, et al. Combined heat and power dispatch considering advanced adiabatic compressed air energy storage for wind power accommodation. *Energy Conversion and Management*. 2019; 200: 112091. Available from: https://doi.org/10.1016/j.enconman.2019.112091.

[17] Jiang R, Yin H, Peng K, Xu Y. Multi-objective optimization, design and performance analysis of an advanced trigenerative micro compressed air energy storage system. *Energy Conversion and Management*. 2019; 186: 323-333. Available from: https://doi.org/10.1016/j.enconman.2019.02.071.

[18] Salvini C. CAES systems integrated into a gas-steam combined plant: Design point performance assessment. *Energies*. 2018; 11(4): 415. Available from: https://doi.org/10.3390/en11020415.

[19] Karam T, Maatouk C. Wind-driven scheduling of compressed air and latent heat storage for optimal gas turbines operation. In: *2021 IEEE 3rd International Multidisciplinary Conference on Engineering Technology*. Beirut, Lebanon: IEEE; 2021. p.173-178. Available from: https://doi.org/10.1109/IMCET53404.2021.9665631.

[20] European Association for storage of energy (EASE). Adiabatic compressed air energy storage. *Energy Storage Technology Descriptions*. Available from: https://ease-storage.eu/wp-content/uploads/2016/03/EASE_TD_ACAES.pdf [Accessed 23th June 2024].

[21] ANSYS Inc. *Ansys® Fluent® Release 2024 R1*. 2024.

[22] Zhou C, Wu S. Medium-and high-temperature latent heat thermal energy storage: Material database, system review, and corrosivity assessment. *International Journal of Energy Research*. 2019; 43(1): 621-661. Available from: https://doi.org/10.1002/er.4216.

[23] Villada C, Ding W, Bonk A, Bauer T. Engineering molten MgCl2-KCl-NaCl salt for high-temperature thermal energy storage: Review on salt properties and corrosion control strategies. *Solar Energy Materials and Solar Cells*. 2021; 230: 111344. Available from: https://doi.org/10.1016/j.solmat.2021.111344.

[24] Lu J, Yang S, Rong Z, Pan G, Ding J, Liu S, et al. Thermal properties of KCl-MgCl2 eutectic salt for high-temperature heat transfer and thermal storage system. *Solar Energy Materials and Solar Cells*. 2021; 228: 111130. Available from: https://doi.org/10.1016/j.solmat.2021.111130.

[25] Zhao W, Zheng Y, Sabol JC, Tuzla K, Neti S, Oztekin A, et al. High temperature calorimetry and use of magnesium chloride for thermal energy storage. *Renewable Energy*. 2013; 50: 988-993. Available from: https://doi.org/10.1016/j.renene.2012.08.036.

[26] Sheng N, Zhu H, Zhang L, Zeng L, Zhu C. Macroencapsulation of sodium chloride by a double layer strategy for high temperature phase change thermal storage over 800 °C. *Journal of Energy Storage*. 2024; 77: 109896. Available from: https://doi.org/10.1016/j.est.2023.109896.

[27] Arconada N, Arribas L, Lucio B, González-Aguilar J, Romero M. Macroencapsulation of sodium chloride as phase change materials for thermal energy storage. *Solar Energy*. 2018; 167: 1-9. Available from: https://doi.org/10.1016/j.solener.2018.02.045.

[28] Bahri CNACZ, Al-Areqi WM, Ruf MIFM, Majid AA. Characteristic of molten fluoride salt system LiF-BeF$_2$ (Flibe) and LiF-NaF-KF (flinak) as coolant and fuel carrier in molten salt reactor (MSR). *AIP Conference Proceedings*. 2017; 1799: 040008. Available from: https://doi.org/10.1063/1.4972932.

[29] Tasidou KA, Magnusson J, Munro T, Assael MJ. Reference correlations for the viscosity of molten LiF-NaF-KF, LiF-BeF$_2$, and Li$_2$CO$_3$-Na$_2$CO$_3$-K$_2$CO$_3$. *Journal of Physical and Chemical Reference Data*. 2019; 48(3): 033101. Available from: https://doi.org/10.1063/1.5131349.

[30] Williams DF, Toth LM, Clarno KT. *Assessment of Candidate Molten Salt Coolants for the Advanced High-Temperature Reactor (AHTR)*. Tennessee: Oak Ridge National Laboratory; 2006. Available from: https://info.ornl.gov/sites/publications/Files/Pub57476.pdf [Accessed 20th December 2024].

[31] Liu TL, Liu WR, Xu XH. Properties and heat transfer coefficients of four molten-salt high temperature heat transfer fluid candidates for concentrating solar power plants. *IOP Conference Series: Earth and Environmental Science*. 2017; 93: 012023. Available from: https://doi.org/10.1088/1755-1315/93/1/012023.

[32] PCM Products Ltd. *PlusICE Range*. Available from: https://www.pcmproducts.net/files/PlusICE%20Range%202021-1.pdf [Accessed 20th December 2024].

[33] Barnes J, Coutts R, Horne T, Thai J. Characterisation of molten salts for their application to molten salt reactors. *PAM Review Energy Science & Technology*. 2019; 6: 38-55. Available from: https://doi.org/10.5130/pamr.v6i0.1546.

[34] Yang L, Xu H, Cola F, Akhmetov B, Gil A, Cabeza LF, et al. Shell-and-tube latent heat thermal energy storage design methodology with material selection, storage performance evaluation, and cost minimization. *Applied Sciences*. 2021; 11(9): 4180. Available from: https://doi.org/10.3390/app11094180.

[35] Tubular Exchanger Manufacturers Association (TEMA). *Standards of the Tubular Exchanger Manufacturers Association*. Tarrytown, NY: TEMA; 2007.

[36] Moran MJ, Shapiro HN, Boettner DD, Bailey MB. *Fundamentals of Engineering Thermodynamics*. 9th ed. Hoboken: John Wiley & Sons; 2018.

[37] Kays WM, London AL. *Compact Heat Exchangers*. 3rd ed. New Delhi: Scientific International Pvt. Ltd.; 2018.

[38] Kakaç S, Liu H, Pramuanjaroenkij A. *Heat Exchangers Selection, Rating, and Thermal Design*. 3rd ed. Boca Raton, FL: CRC Press; 2012.

[39] Di Bono G, Corcione M, Quintino A. Systematic comparative analysis of Kern and Bell-Delaware methods for the design of shell-and-tube heat exchangers. *Applied Thermal Engineering*. 2025; 278: 127327. Available from: https://doi.org/10.1016/j.applthermaleng.2025.127327.

[40] Kern DQ. *Process Heat Transfer*. New York: McGraw-Hill; 1950.

[41] Serth RW. *Process Heat Transfer: Principles and Applications*. Amsterdam: Elsevier Science & Technology Books; 2007.

[42] Spalding DB, Taborek J. *Heat Exchanger Theory*. Washington, DC: Hemisphere Publishing Corporation; 1983.

[43] GAMS Development Corp./GAMS Software GmbH. *The General Algebraic Modeling System (GAMS)*. Available from: https://www.gams.com/ [Accessed 26th May 2025].

[44] GAMS Development Corp. USA. *CONOPT Home Page*. Available from: https://www.gams.com/products/conopt/ [Accessed 26th May 2025].

[45] ANSYS Inc. *Ansys® SpaceClaim® Release 2024 R1*. 2024.

[46] Siemens Energy. SGT-400 Gas Turbine. Available from: https://www.siemens-energy.com/global/en/home/products-services/product/sgt-400.html [Accessed 5th December 2024].

[47] Janz GJ. *Molten Salts Handbook*. Amsterdam: Elsevier; 1967. Available from: https://doi.org/10.1016/B978-0-123-95642-2.X5001-1.

[48] Oak Ridge National Laboratory. The Molten Salt Thermochemical Database (MSTDB). Available from: https://www.ornl.gov/ [Accessed 18th December 2024].

[49] Zeneli M, Nikolopoulos A, Karellas S, Nikolopoulos N. Numerical methods for solid-liquid phase-change problems. In: *Ultra-High Temperature Thermal Energy Storage, Transfer and Conversion*. Amsterdam: Elsevier; 2020. p.165-199. Available from: https://doi.org/10.1016/B978-0-12-819955-8.00007-7.

[50] ANSYS Inc. *Ansys® Fluent®, Release 2024 R1, Help System, Fluent Theory Guide, Chapter 17. Solidification and Melting*. 2024. Available from: https://www.afs.enea.it/project/neptunius/docs/fluent/html/th/node349.htm [Accessed 18th December 2024].

Appendix A

Table 5. Air outlet temperature MAPE & PCM liquid fraction RMSE

Case	PCM ref.	$T_{air,\, in}$ (K)	$\dot{m}_{air,\, in}$ (kg/s)	$p_{air,\, in}$ bar	Ste	Mode	$T_{air,\, in}$ MAPE			Liquid fraction RMSE		
							Taborek	Kern	Bell-delaware	Taborek	Kern	Bell-delaware
1	PCM1	350	44	17	0.641	DISCH	0.3%	0.6%	1.7%	0.038	0.010	0.090
2	PCM1	350	44	12	0.641	DISCH	0.3%	0.6%	1.7%	0.037	0.009	0.091
3	PCM1	873	44	17	0.448	CH	0.2%	0.4%	0.6%	0.022	0.011	0.076
4	PCM1	700	44	17	0.087	CH	0.06%	0.18%	0.5%	0.020	0.004	0.040
5	PCM2	350	44	17	0.816	DISCH	0.4%	0.6%	1.7%	0.025	0.015	0.092
6	PCM2	873	44	17	0.376	CH	0.2%	0.3%	0.6%	0.021	0.009	0.067
7	PCM2	750	44	17	0.095	CH	0.07%	0.17%	0.42%	0.018	0.003	0.041
8	PCM3	600	44	17	0.824	DISCH	0.4%	0.4%	0.5%	0.015	0.025	0.049
9	PCM3	600	44	25	0.824	DISCH	0.4%	0.4%	0.5%	0.015	0.024	0.049
10	PCM3	350	44	17	1.356	DISCH	0.9%	0.9%	1.2%	0.034	0.045	0.075
11	PCM4	350	44	17	1.659	DISCH	2.0%	2.1%	3.0%	0.043	0.061	0.115
12	PCM5	350	44	17	0.856	DISCH	0.6%	1.0%	5.7%	0.075	0.025	0.156
13	PCM5	350	30	17	0.856	DISCH	0.6%	2.6%	7.7%	0.049	0.016	0.180
14	PCM5	873	44	17	0.332	CH	0.1%	0.6%	1.7%	0.047	0.009	0.100
15	PCM5	800	44	17	0.165	CH	0.03%	0.36%	1.14%	0.031	0.004	0.056
16	PCM5	800	30	17	0.165	CH	0.18%	0.62%	1.46%	0.015	0.007	0.050
17	PCM6	350	44	17	1.471	DISCH	0.8%	0.8%	1.4%	0.022	0.035	0.083
18	PCM6	350	20	17	1.471	DISCH	0.9%	1.7%	3.3%	0.024	0.051	0.106
19	PCM6	873	44	17	0.306	CH	0.2%	0.2%	0.4%	0.009	0.008	0.036
20	PCM7	350	44	17	1.506	DISCH	0.7%	0.8%	1.4%	0.026	0.044	0.102
21	PCM7	873	44	17	0.473	CH	0.1%	0.2%	0.4%	0.012	0.009	0.050
22	PCM8	350	44	17	2.830	DISCH	1.6%	1.5%	2.6%	0.054	0.081	0.160
23	PCM9	350	44	17	1.936	DISCH	1.1%	1.0%	3.1%	0.033	0.051	0.165
24	PCM9	500	44	17	1.029	DISCH	0.1%	0.4%	1.3%	0.031	0.023	0.138
25	PCM9	873	44	17	1.228	CH	0.2%	0.4%	0.9%	0.022	0.054	0.143
26	PCM9	700	44	17	0.181	CH	0.02%	0.13%	0.48%	0.025	0.007	0.041
27	PCM10	350	44	17	4.666	DISCH	1.8%	1.8%	2.0%	0.111	0.129	0.182
28	PCM11	350	44	17	2.428	DISCH	1.4%	1.4%	1.9%	0.058	0.078	0.135
29	PCM12	350	50	17	4.509	DISCH	2.9%	2.9%	3.3%	0.108	0.126	0.179
30	PCM12	350	44	17	4.509	DISCH	3.0%	3.0%	3.4%	0.111	0.130	0.185
31	PCM13	350	44	17	1.268	DISCH	0.1%	0.1%	0.3%	0.018	0.026	0.091